Minority carrier lifetime and dark current measurements in mid-wavelength infrared InAs_{0.91}Sb_{0.09} alloy nBn photodetectors

B.V. Olson, ^{a)} J.K. Kim, E.A. Kadlec, J.F. Klem, S.D. Hawkins, D. Leonhardt, W.T. Coon, T.R. Fortune, M. Cavaliere, A. Tauke-Pedretti, and E.A. Shaner

Sandia National Laboratories, Albuquerque, New Mexico 87185, USA

Carrier lifetime and dark current measurements are reported for a mid-wavelength infrared InAs_{0.91}Sb_{0.09} alloy nBn photodetector. Minority carrier lifetimes are measured using a non-contact time-resolved microwave technique on unprocessed portions of the nBn wafer and the Auger recombination Bloch function parameter is determined to be $|F_1F_2| = 0.292$. The measured lifetimes are also used to calculate the expected diffusion dark current of the nBn devices and compared to the experimental dark current measured in processed photodetector pixels from the same wafer. Excellent agreement is found between the two, highlighting the important relationship between lifetimes and diffusion currents in nBn photodetectors.

^{a)}Email: benolso@sandia.gov

Due primarily to the wide variety in bandgap energies and electron affinities, the 6.1 Å lattice constant family of semiconductors, namely InAs, GaSb, AlSb, and related alloys and quaternaries, is used extensively to engineer novel infrared (IR) heterostructures and barrier devices¹. One such architecture is the nBn photodetector, which utilizes a thick *n*-type IR absorbing layer separated from a top *n*-type contact layer by a wide-bandgap electron barrier layer². The nBn is therefore a minority carrier device, where the holes are able to flow unimpeded throughout the structure. The primary benefit of the nBn architecture is it can significantly reduce depletion region related generation-recombination (GR) currents in materials prone to Shockley-Read-Hall (SRH) defects, such as the aforementioned III-V materials.

One of the most critical metrics of a photodetector is the dark current as this ultimately determines the detectivity and operating temperature for a given acceptable performance. For modest biases and temperatures, there are two primary sources of dark current in a nBn detector. The first is diffusion current (J_{diff}) arising from thermal generation of carriers in the thick, undepleted n-type IR absorbing layer. A simplified expression is³,

$$J_{diff} = q \frac{n_i^2 W}{n_o \tau_{mc}} \tag{1}$$

where q is the electron charge, n_o is the majority carrier electron density (i.e. the absorber doping level), n_i is the intrinsic carrier density, W is the width of the absorber or the minority carrier diffusion length, whichever is smaller, and τ_{mc} is the minority carrier lifetime. The second is GR current (J_{GR}) arising from the portion of the absorber that becomes depleted under bias. A simplified expression for GR current is,

$$J_{GR} = q \frac{n_i W_{dep}}{\tau_{no} + \tau_{po}} \tag{2}$$

where W_{dep} is the depletion thickness and τ_{no} and τ_{po} are SRH specific carrier lifetimes⁴. These

equations emphasize the important relationship between the carrier lifetime dynamics in the narrow-bandgap IR absorber layer and the more tangible detector dark current in a nBn photodetector.

Here, electrical and τ_{mc} measurements are reported for the same MWIR InAs_{0.91}Sb_{0.09} alloy nBn wafer. By making measurements on the same wafer, better correlation between τ_{mc} and J_{diff} can be made. Lattice matched to GaSb at a Sb composition of approximately 9%, InAs_{1-x}Sb_x has been shown to extend out to the long-wave infrared spectral region for larger fractions of Sb, where bandgaps as small as 120 meV have been demonstrated⁵. Growth of InAs_{1-x}Sb_x has also been demonstrated on both GaSb and GaAs substrates^{6,7}. Furthermore, InAs_{1-x}Sb_x nBn detectors have shown impressive performances, both as single pixel⁸ and as large format focal plane arrays (FPAs)^{9,10}. Recently, long τ_{mc} have been reported indicating high material quality¹¹. While these reports highlight why InAs_{1-x}Sb_x nBn detectors are a competitive alternative for IR detection, correlating the nonequilibrium charge carrier characteristics of this material system to device performance is needed in order to understand material limitations.

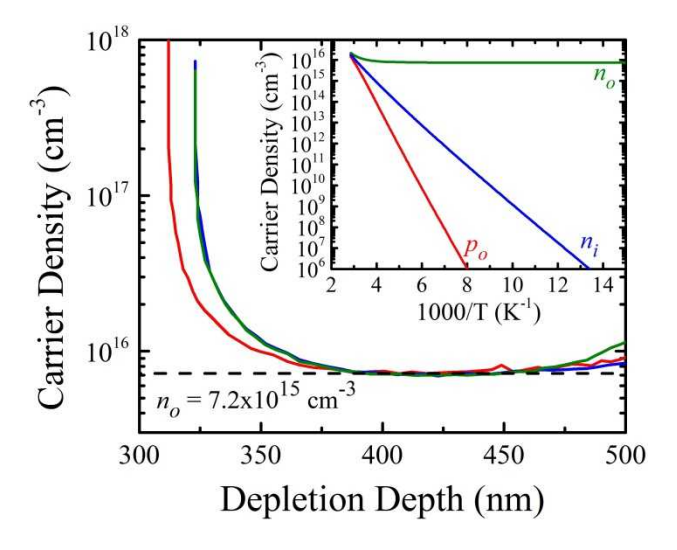


FIG. 1. Equilibrium electron concentrations as a function of depletion depth into the absorber layer (solid curves), determined from analysis of capacitance-voltage data on a few nBn devices. For

depletion widths greater than 350 nm, the carrier density reflects the equilibrium electron concentration in the $InAs_{0.91}Sb_{0.09}$ absorber layer (dashed curve). The inset shows calculated majority electron (n_o), minority hole (p_o), and intrinsic (n_i) carrier densities as a function of temperature for $InAs_{0.91}Sb_{0.09}$ at the measured doping level.

The nBn sample was grown by molecular beam epitaxy on a (100)-oriented tellurium doped GaSb substrate. The epitaxial growth layers consist of a buffer layer and bottom contact structure, a 4 µm thick InAs_{0.91}Sb_{0.09} IR absorber layer intentionally doped using silicon, a 100 nm thick AlAsSb electron barrier layer, and a 100 nm thick n-type InAsSb top contact layer. The absorber bandgap energy is approximately 320 meV (3.9 µm) at 100 K. Portions of the wafer were fabricated into test photodetector pixels using standard processing and packaging techniques. Photolithography and wet chemical etching were used to etch mesas into the top contact layer to the electron barrier layer, defining photodetector pixels. Contact to the absorber was made by etching through the electron barrier and absorber layers to the bottom contact. These test devices were packaged, wire bonded, and housed in a cryostat for the electrical measurements. Capacitance-voltage (CV) measurements, taken in a similar manner as described by Klem et al.²⁰, are used to determine n_o of the InAs_{0.91}Sb_{0.09} absorber. These data are shown in Fig. 1 for a few representative nBn diodes from the sample wafer, each confirming n_a of approximately 7.2×10^{15} cm⁻³ at 100 K in the absorber. Using this value for n_0 , 14-band $\mathbf{k} \cdot \mathbf{p}$ software¹⁹ is then used to calculate the temperature dependence of n_o , n_i , and p_o , the results of which are shown in the inset to Fig. 1.

Carrier lifetimes are reported using a non-contact and non-destructive time-resolved microwave reflectance (TMR) method on unprocessed portions of the sample wafer. This apparatus consists of an optical parametric oscillator, which produces tunable nanosecond IR

pulses of light and is used to optically generate excess carriers in the narrow-bandgap absorber layer. By tuning the pump wavelength to the absorber bandgap energy (in this case a wavelength of 3.7 μ m is used), a near uniform distribution of excess carriers can be generated through the thick absorber. On a time scale fast compared to recombination, these excited carriers relax to the absorber band edge states and alter the conductivity. Microwave radiation reflected from the sample probes this change in conductivity and thus the excited carrier population¹². The subsequent decay of the excess carriers back to equilibrium, and therefore the carrier lifetime, is temporally resolved by monitoring the change in reflected microwave power as a function of time.

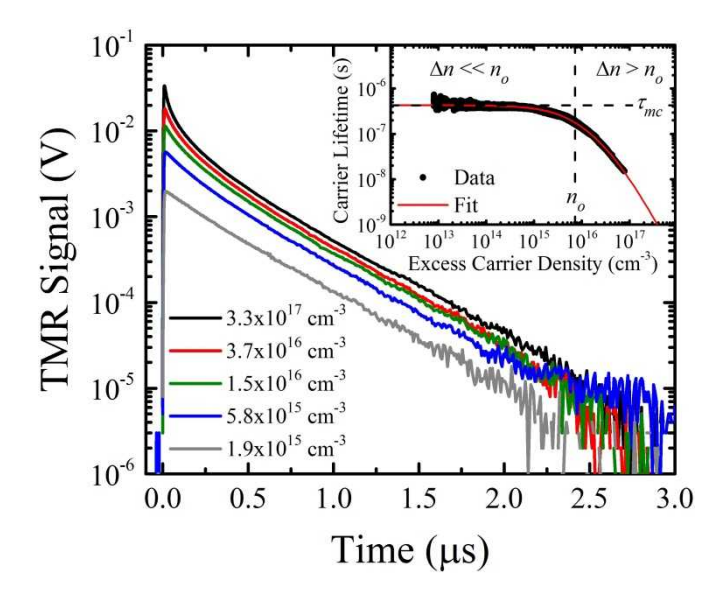


FIG. 2. 100 K time-resolved microwave decays for different initial optically generated excess carrier densities. The inset shows the resulting carrier lifetimes as a function of the excess carrier density by calibrating the instantaneous rate of decay of the TMR decay data (symbols). The solid red curve is a best fit to the lifetime data. The vertical dashed line corresponds to the doping level of the nBn devices and the horizontal dashed line corresponds to the minority carrier lifetime.

Example TMR decay data from the nBn sample, taken at a temperature of 100 K, are

shown in Fig. 2 for multiple different initial optically generated carrier densities. These decay curves are transformed into instantaneous carrier lifetimes as a function of excess carrier density (Δn) using calibrated analysis methods described previously 11,14,15. The resulting instantaneous carrier lifetime data are shown in the inset to Fig. 2. For Δn values that are greater than the doping level n_o (i.e. the high injection regime) the carrier lifetime is short, on the order to tens of nanoseconds, and is where the Auger recombination coefficient, C_n , is determined. This corresponds to the rapid decay at short time scales and large injected carrier densities in the decay curves. As Δn decreases through carrier recombination, the lifetime lengthens and reaches a constant value for $\Delta n << n_o$. We determine τ_{mc} from this low injection lifetime data using a density-dependent lifetime fitting model¹³. For the 100 K data shown here, $\tau_{mc} = 430\pm20$ ns and $C_n = 6 \times 10^{-27} \text{ cm}^6/\text{s}$. As described in Ref. 13, the absorber doping level is explicitly taken into account during the fitting of this data. This can be done in two ways, where the first is to fix n_o using the measured values from Fig. 1. Here, however, we allow n_o to be a free parameter during the fitting routine in order to assess the accuracy of using calibrated lifetime data to determine the absorber's doping level. Allowing this value to vary for the best fit provides $n_o = 6 \times 10^{15}$ cm⁻³, which has very good agreement with n_o measured from CV analysis (7.2x10¹⁵ cm⁻³). This result indicates that careful analysis of carrier lifetime data in this manner can be an accurate measurement of the doping level in narrow-bandgap material. This procedure of measuring and fitting carrier lifetime data is repeated for temperatures ranging from 80 K to 350 K and the resulting τ_{mc} values are plotted in Fig. 3. Here, τ_{mc} decreases slightly from 550 ns at 80 K to 300 ns at 300 K. At greater temperature, a steep decline in τ_{mc} is observed.

Previous analysis by us for a similarly doped InAs_{0.91}Sb_{0.09} alloy showed that Auger recombination limits τ_{mc} across a wide range of temperatures¹⁶. The analysis described therein includes effects of radiative, SRH, and Auger recombination to make this conclusion. With this in

mind, we limit ourselves here to only comparing the measured τ_{mc} to the predicted Auger lifetime. From the theory of Beattie, Landsberg, and Blakemore (BLB) the Auger lifetime can be modeled using 17,18 ,

$$\tau_{auger} = \frac{2n_i^2}{n_o^2 + n_o p_o} \tau_{A1}^{(i)} \tag{3}$$

where the intrinsic Auger-1 lifetime is,

$$\tau_{A1}^{(i)} = 3.8 \times 10^{-18} \frac{\varepsilon_{\infty}^{2} (1+\mu)^{1/2} (1+2\mu)}{(m_e/m_o)|F_1F_2|^2} \left(\frac{E_g}{k_B T}\right)^{3/2} exp\left(\frac{1+2\mu}{1+\mu} \frac{E_g}{k_B T}\right) \tag{4}$$

where ε_{∞} the high frequency dielectric constant, $\mu = m_e/m_h$, m_e is the electron effective mass, m_h is the hole effective mass, m_o is the free electron mass, $|F_1F_2|$ is the Bloch function overlap parameter, k_B is Boltzmann's constant, and T is the temperature. In the case of Ref. 16, lifetime data are reported up to a temperature of 300 K. The onset of the intrinsic temperature range, subsequent large intrinsic densities, and steep decline in τ_{mc} due to $\tau_{A1}^{(i)}$ is therefore not observed in our previous data. Here, lifetime data are reported up to 350 K in order to better define $|F_1F_2|$, which is a critical parameter determining the intrinsic Auger recombination lifetime and ultimately the best case nonradiative carrier lifetime. Using effective masses of $m_e = 0.027$ and $m_h = 0.405$, calculated using the 14-band $\mathbf{k} \cdot \mathbf{p}$ software, and $\varepsilon_{\infty} = 12.6$, $\tau_{A1}^{(i)}$ fits well to the high temperature data using $|F_1F_2| = 0.292$.

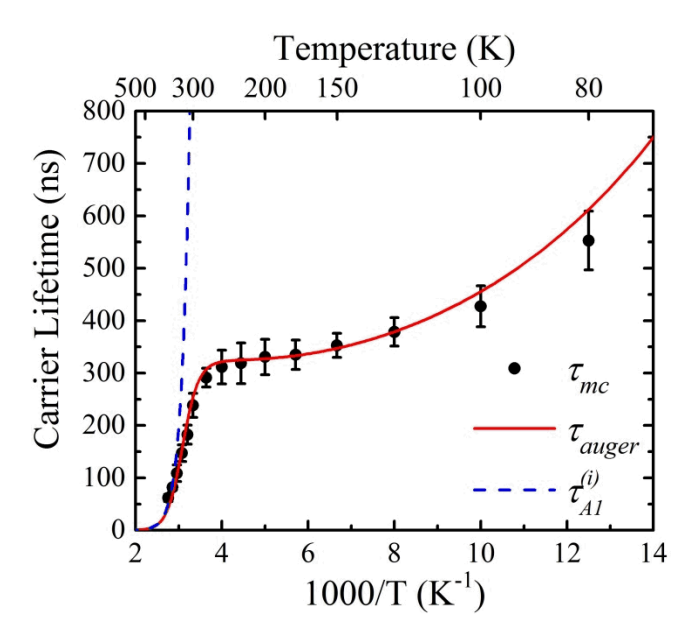


FIG 3. Measured minority carrier lifetimes (symbols) as a function of temperature. The curves are the BLB Auger (τ_{auger}) and intrinsic Auger-1 ($\tau_{A1}^{(i)}$) lifetimes^{17,18} fitted to the data.

Using with the carrier density data from Fig. 1 and the refined $|F_1F_2|$ value, τ_{auger} can be determined with Eq. 3. This calculated BLB Auger lifetime, also shown in Fig. 3, follows closely with the measured τ_{mc} values, indicating that the SRH and radiative recombination are not significant contributors to the total minority carrier lifetime for this doping level, in accordance with our previous reports¹⁶. This however does not preclude the existence of SRH defects and subsequent GR current, only that Auger recombination is the recombination mechanism controlling τ_{mc} at this doping level. Interestingly, an Auger limited τ_{mc} puts restrictions on the optimal doping level for a photodetector. In terms of the Auger coefficient, Eq. 3 is re-written as,

$$\tau_{auger} = \frac{1}{C_n(n_o^2 + n_o p_o)} \tag{4}$$

with,

$$C_n = \frac{1}{2n_i^2 \tau_{A1}^{(i)}} \tag{5}$$

If we consider *n*-type material, Eq. 4 is simply $1/(C_n n_o^2)$. According to Eq. 1 then, increased

doping combined with an Auger limited minority carrier lifetime leads to a linear increase in the J_{diff} component of the dark current. For diffusion limited detectors, smaller dark current can therefore be attained by decreasing the doping level during growth and the potential impact on the dark current can be predicted through minority carrier lifetime characterization.

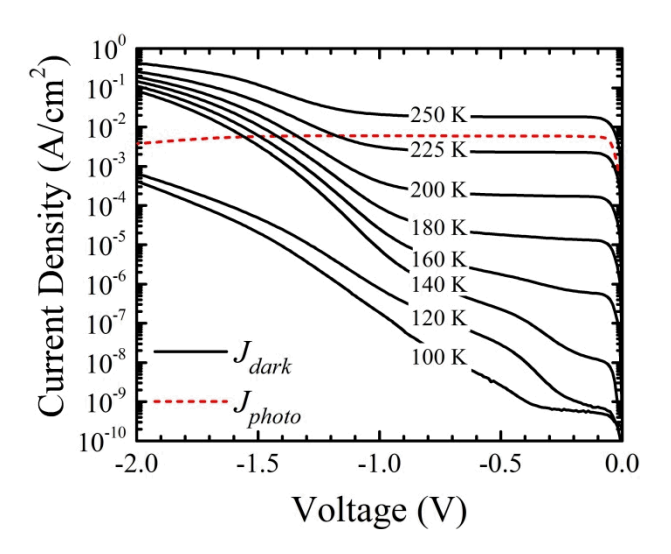


FIG. 4. Dark current versus voltage characteristics of the InAs_{0.91}Sb_{0.09} nBn photodetector (solid curves) as a function of temperature, where negative voltages correspond to reverse bias. The dashed curve is 100 K photocurrent.

Fig. 4 shows experimental dark current as a function of reverse bias and temperature for a typical nBn device from the wafer. Also shown is the 100 K nBn photocurrent, which is observed to require a relatively small bias of -0.1 V to reach saturation. This specifies that maximum extraction of the photo-generated carriers occurs by this voltage and that diffusion current from the absorber is fully collected by this bias as well. An Arrhenius plot is shown in Fig. 5 for reverse biases of -0.1 V, -0.5 V, -1.0 V. Typically, these data are fitted at a particular bias to extract the slopes and the activation energies, which when compared to the temperature dependencies of Eqs. 1 and 2 can determine the limiting behavior of the dark current. Here, we provide a comparison

between the experimental dark current and J_{diff} determined from the independently measured τ_{mc} using Eq. 1. This calculated diffusion current is shown in Fig. 5 as the solid curve. Excellent agreement is observed between the two, indicating that the nBn devices are indeed diffusion limited at a bias of -0.1 V and that non-destructive measurement of carrier lifetimes can provide useful insight into actual device performance. As the reverse bias is increased, GR current is observed to turn on at low temperatures as the depletion layer begins to incorporate a portion of the narrow-bandgap InAs_{0.91}Sb_{0.09} absorber layer. From Eq. 2, it is noted that J_{GR} is linearly dependent on n_i and the temperature dependence is therefore proportional to $T^{3/2}exp(-E_g/2k_BT)$. J_{GR} is noted by the dashed curve in Fig. 5. This curve is not a fit to the data, but merely a guide to show the slope of J_{GR} and at what biases and temperatures it dominates the dark current.

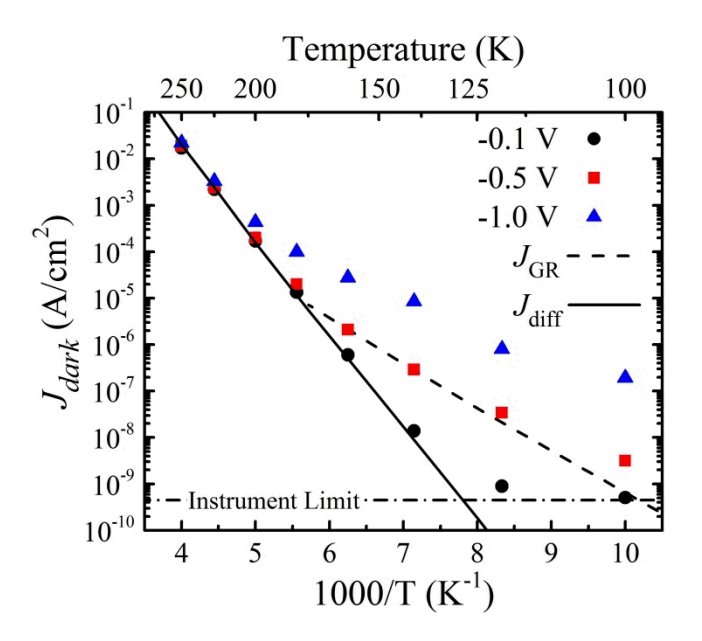


FIG. 5. Measured dark current as a function of temperature (symbols) for a few different biases, with the bias of -0.1 V corresponding to the minimum voltage necessary to fully extract the photocurrent from the absorber. For temperatures less than 120 K, the dark current is less than the instrument capabilities at the bias of -0.1 V. The solid curve is the independently calculated diffusion current found using the measured minority carrier lifetime data. The dashed curve

corresponds to the trend GR current has with temperature.

In summary, electrical and optical measurements were reported for a MWIR InAs_{0.91}Sb_{0.09} nBn photodetector. From fabricated test photodetector pixels, dark current and photocurrent were reported. CV measurements were also reported, providing a measurement of the equilibrium electron (majority carrier) concentration in the InAs_{0.91}Sb_{0.09} absorber, which was found to be 7.2 \times 10¹⁵ cm⁻³. Using a non-contact time-resolved microwave reflectance technique, carrier lifetimes were measured for the same nBn wafer and used to extract τ_{mc} as a function of temperature. Comparing the τ_{mc} data with Auger lifetime theory indicates that Auger recombination limits the minority carrier lifetime dynamics at this doping level. A value for $|F_1F_2|$ of 0.292, which is a critical parameter determining the Auger-1 lifetime, was determined from high temperature τ_{mc} data. Combined with carrier density data, the τ_{mc} values were used to calculate the diffusion current and compared to the actual experimental dark current. Excellent agreement was found between these. This expresses not only the important relationship between the underlying nonequilibrium charge carrier dynamics and nBn device performance, but also the utility of non-contact and nondestructive measurement of carrier lifetimes as it can be linked directly to potential device diffusion current. Additionally, the TMR method used here is very sensitive, capable of measuring both doped and undoped material, is bandgap insensitive, and is amenable to spatially mapping τ_{mc} over entire wafers in reasonable time. This is therefore useful technology for wafer diagnostics and purging before the commitment is made for processing and fabrication into FPAs. It was also shown that analysis of the calibrated carrier lifetime data allows for accurate extraction of the absorber's doping level, another critical value in determining the diffusion current. It is therefore possible to attain both τ_{mc} and n_o from a single non-destructive measurement.

This project was supported by a grant from the Intelligence Community Postdoctoral

Research Fellowship Program through funding from the Office of the Director of National Intelligence. All statements of fact, opinion, or analysis expressed are those of the author and do not reflect the official positions or views of the Intelligence Community or any other U.S. Government agency. Nothing in the contents should be construed as asserting or implying U.S. Government authentication of information or Intelligence Community endorsement of the author's views. The authors would also like to thank Michael Flatte at the University of Iowa for use of his **k•p** software.

Sandia National Laboratories is a multi-program laboratory managed and operated by Sandia Corporation, a wholly owned subsidiary of Lockheed Martin Corporation, for the U.S. Department of Energy's National Nuclear Security Administration under contract DE- AC04-94AL85000.

REFERENCES

¹P. Martyniuk, J. Antoszewski, M. Martyniuk, L. Faraone, and A. Rogalski. *Appl. Phys. Rev.*, **1**, 041102 (2015).

²S. Maimon and G. W. Wicks. *Appl. Phys. Lett.*, **89**, 151109 (2006).

³D. R. Rhiger. J. Electron. Mat., **40**, 1815–1822 (2011).

⁴C.-T. Sah, R. N. Noyce, and W. Shockley. *Proc. of IRE*, **45**, 1228–1248 (1957).

⁵S.P. Svensson, W. L. Sarney, H. Hier, Y. Lin, D. Wang, D. Donetsky, L. Shterengas, G. Kipshidze, and G. Belenky. *Phys. Rev. B* **86**, 245205 (2012).

⁶J. M. Fastenau, D. Lubyshev, Y. Qiu, A. W. K. Liu, E. J. Koerperick, J. T. Olesberg, and D. Norton. *J. Vac. Sci. Technol. B*, **31**, 03C106 (2013).

⁷E. Weiss, O. Klin, S. Grossmann, N. Snapie, I. Lukomsky, D. Aronov, M. Yassen, E. Berkowicz, A. Glozman, P. Klipstein, A. Fraenkel, and I. Shtichman. *J. Crystal Growth*, **339**, 31–35 (2012).

- ⁸A. Soibel, C. Hill, S. Keo, L. Hoglund, R. Rosenberg, R. Kowalczyk, A. Khoshakhalgh, A. Fisher, D.-Z. Ting, and S. Gunapala. *Appl. Phys. Lett.*, **105**, 023512 (2014).
- ⁹E. Robinson, A. I. D'Souza, A. C. Ionescu, D. Okerlund, T. J. de Lyon, R. D. Rajavel,
 H. Sharifi, N. K. Dhar, P. S. Wijewarnasuriya, and C. Grein. *Proc. of SPIE*, 9220,
 92200D (2014).
- 10Y. Karni, E. Avnon, M. B. Ezra, E. Berkowicz, O. Cohen, Y. Cohen, R. Dobromislin, I. Hirsh,
 O. Klin, P. Klipstein, I. Lukomsky, M. Nitzani, I. Pivnik, O. Rozenberg, I. Shtrich-man, M. Singer, S. Sulimani, A. Tuito, and E. Weiss. *Proc. of SPIE*, **9070**, 90701F (2014).
- ¹¹B. V. Olson, E. A. Shaner, J. K. Kim, J. F. Klem, S. D. Hawkins, L. M. Murray, J. P. Prineas, M. E. Flatt'e, and T. F. Boggess. *Appl. Phys. Lett.*, **101**, 092109 (2012).
- ¹²M. Kunst and G. Beck. *J. Appl. Phys.*, **60**, 3558 (1986).
- ¹³B. V. Olson, E. A. Kadlec, J. K. Kim, S. D. Hawkins, E. A. Shaner, and M. E. Flatt'e. *Submitted to Phys. Rev. Appl.*
- ¹⁴M. E. Flatt'e, C. H. Grein, T. C. Hasenberg, S. A. Anson, D.-J. Jang, J. T. Olesberg, and T. F. Boggess. *Phys. Rev. B*, **59**, 5745–5750 (1999).
- ¹⁵Y. Aytac, B. V. Olson, J. K. Kim, E. A. Shaner, S. D. Hawkins, J. F. Klem, M. E. Flatt'e, and T. F. Boggess. *Appl. Phys. Lett.*, **105**, 022107 (2014).
- ¹⁶B. V. Olson, E. A. Shaner, J. K. Kim, J. F. Klem, S. D. Hawkins, M. E. Flatt'e, and T. F. Boggess. *Appl. Phys. Lett.*, **103**, 052106 (2013).
- ¹⁷A. R. Beattie and P. T. Landsberg. *Proc. of Royal Soc.*, **249**, 16–29 (1959).
- ¹⁸J. Blakemore. *Semiconductor Statistics*. Dover Publications, Inc., Mineola, New York (1962).
- ¹⁹W. H. Lau, J. T. Olesberg, and M. E. Flatt'e. *Cond-Mat/0406201*.
- ²⁰J. F. Klem, J. K. Kim, M. J. Cich, S. D. Hawkins, T. R. Fortune, and J. L. Rienstra. *Proc. of SPIE*, **7608**, 76081P (2010).